

# CO Gas Sensing by Ultrathin Tin Oxide Films Grown by Atomic Layer Deposition Using Transmission FTIR Spectroscopy<sup>†</sup>

X. Du,<sup>‡</sup> Y. Du,<sup>§</sup> and S. M. George<sup>\*,‡,§</sup>

Departments of Chemical and Biological Engineering and of Chemistry and Biochemistry,  
University of Colorado, Boulder, Colorado 80309

Received: January 18, 2008; Revised Manuscript Received: June 27, 2008

Ultrathin tin oxide films were deposited on SiO<sub>2</sub> nanoparticles using atomic layer deposition (ALD) techniques with SnCl<sub>4</sub> and H<sub>2</sub>O<sub>2</sub> as the reactants. These SnO<sub>x</sub> films were then exposed to O<sub>2</sub> and CO gas pressure at 300 °C to measure and understand their ability to serve as CO gas sensors. In situ transmission Fourier transform infrared (FTIR) spectroscopy was used to monitor both the charge conduction in the SnO<sub>x</sub> films and the gas-phase species. The background infrared absorbance measured the electrical conductivity of the SnO<sub>x</sub> films based on Drude–Zener theory. O<sub>2</sub> pressure was observed to decrease the SnO<sub>x</sub> film conductivity. Addition of CO pressure then increased the SnO<sub>x</sub> film conductivity. Static experiments also monitored the buildup of gas-phase CO<sub>2</sub> reaction products as the CO reacted with oxygen species. These results were consistent with both ionosorption and oxygen-vacancy models for chemiresistant semiconductor gas sensors. Additional experiments demonstrated that O<sub>2</sub> pressure was not necessary for the SnO<sub>x</sub> films to detect CO pressure. The background infrared absorbance increased with CO pressure in the absence of O<sub>2</sub> pressure. These results indicate that CO can produce oxygen vacancies on the SnO<sub>x</sub> surface that ionize and release electrons that increase the SnO<sub>x</sub> film conductivity, as suggested by the oxygen-vacancy model. The time scale of the response of the SnO<sub>x</sub> films to O<sub>2</sub> and CO pressure was also measured by using transient experiments. The ultrathin SnO<sub>x</sub> ALD films with a thickness of ~10 Å were able to respond to O<sub>2</sub> within ~100 s and to CO within ~10 s. These in situ transmission FTIR spectroscopy help confirm the mechanisms for chemiresistant semiconductor gas sensors.

## I. Introduction

Using the electrical conductivity of semiconductor metal oxides for gas detection started with the original work of Seiyama on ZnO<sup>1</sup> and Taguchi<sup>2</sup> on SnO<sub>2</sub> in the 1960s. Semiconductor metal oxide gas sensors are now commercialized and used in a variety of applications.<sup>3,4</sup> These solid-state gas sensors have many advantages such as small size, low cost, simple operation, and chemical stability. However, there are also corresponding disadvantages such as lack of reproducibility, poor selectivity for specific gases, and insufficient sensitivity.<sup>5</sup> Improving the performance of these gas sensors is difficult because the basic mechanism for gas sensing by these semiconductor metal oxides is still under active debate.<sup>6</sup>

The semiconductor metal oxides function as gas sensors because their electrical conductivity is dependent on gas adsorption. There are two main mechanisms proposed for the semiconductor metal oxide gas sensors based on the ionosorption model and oxygen-vacancy model. Both of these models can be used to interpret gas sensor response, and both may be applicable at the same time. According to the ionosorption model,<sup>7–10</sup> O<sub>2</sub> traps conduction electrons on the surface as ionosorbed oxygen species (O<sub>2</sub><sup>−</sup>, O<sup>−</sup>, O<sup>2−</sup>) and reduces the electrical conductivity. Reducing gases, such as CO, then react with oxygen species to form gaseous CO<sub>2</sub> and increase the electrical conductivity by returning the conduction electrons to the metal oxide film. A schematic illustrating the ionosorption

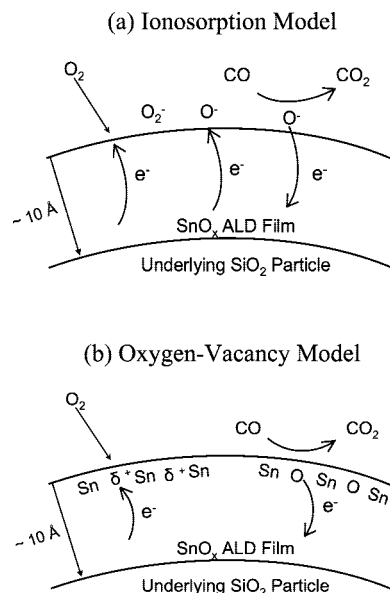


**Figure 1.** Schematic for O<sub>2</sub> interaction and CO gas sensing by SnO<sub>x</sub> film: (a) ionosorption model and (b) oxygen-vacancy model.

model is shown in Figure 1a. The ionosorption model is widely accepted even though spectroscopic investigations have failed to observe the postulated negatively charged oxygen species.<sup>7</sup>

The oxygen-vacancy model is also consistent with most observations for semiconductor metal oxide gas sensors.<sup>8,11</sup> In the oxygen-vacancy model, reducing gases, such as CO, react with oxygen in the surface of the metal oxide to produce gaseous

<sup>†</sup> Part of the "Stephen R. Leone Festschrift".

\* Corresponding author. E-Mail: steven.george@colorado.edu.

<sup>‡</sup> Department of Chemical and Biological Engineering.

<sup>§</sup> Department of Chemistry and Biochemistry.

CO<sub>2</sub>. The oxygen vacancy left behind then ionizes and produces an electron in the conduction band of the metal oxide that increases the electrical conductivity. If O<sub>2</sub> is present, the O<sub>2</sub> can refill the oxygen vacancy and recapture the electron from the conduction band and reduce the electrical conductivity. A schematic illustrating the oxygen-vacancy model is displayed in Figure 1b. The oxygen-vacancy model is not discussed as widely as the ionosorption model even though this model predicts the same changes in electrical conductivity.

An important factor affecting the performance of semiconductor metal oxide gas sensors is the grain size or film thickness.<sup>12–15</sup> The grain size or film thickness is important because a space-charge region, that is, a region affected by a loss or gain of charge carriers, is formed under the surface of either the ionosorbed oxygen species in the ionosorption model or the ionized oxygen vacancies in the oxygen-vacancy model. The depth of the space-charge region is correlated with the Debye length and is typically only several nanometers.<sup>12,16,17</sup> Because the electrical conductivity is only changing approximately over the Debye length, the metal oxide grain size or film thickness plays an important role in determining the sensitivity of the metal oxide gas sensor.<sup>18</sup> Many investigations have revealed that the sensitivity of metal oxide gas sensors increases dramatically when using metal oxide nanoparticles,<sup>13–15,19</sup> nanometer thick films,<sup>12</sup> nanowires,<sup>20,21</sup> or nanobelts.<sup>22</sup>

Experiments that can be performed with precise film thicknesses will be able to overcome the variability in sensitivity produced by the finite Debye length. To take advantage of the higher-sensitivity metal oxide films with nanometer thickness, exact nanometer film thicknesses would be desirable for experimental investigations of metal oxide gas sensors. One technique that can produce very accurate and conformal ultrathin film thicknesses is atomic layer deposition (ALD).<sup>23,24</sup> ALD is a gas-phase fabrication process that is based on sequential, self-limiting surface reactions. ALD can be used to deposit many semiconductor metal oxides used as gas sensors such as SnO<sub>2</sub>,<sup>25–27</sup> ZnO,<sup>28,29</sup> and TiO<sub>2</sub>.<sup>30,31</sup> These semiconductor metal oxides grown by ALD may have many advantages for gas sensors.<sup>32</sup>

In this paper, in situ transmission Fourier transform infrared (FTIR) spectroscopy was utilized to investigate CO gas sensing by ultrathin tin oxide films grown using ALD. CO gas sensing by tin oxide is a model system that has been explored extensively.<sup>14,20–22,33–36</sup> The tin oxide ALD films were deposited on SiO<sub>2</sub> nanoparticles using SnCl<sub>4</sub> and H<sub>2</sub>O<sub>2</sub> as the reactants. Only 16 SnCl<sub>4</sub>/H<sub>2</sub>O<sub>2</sub> reaction cycles were used to deposit a SnO<sub>x</sub> ALD film thickness of ~10 Å that is less than the Debye length for tin oxide.<sup>12</sup> The electrical conductivity of this SnO<sub>x</sub> ALD film was then monitored using background infrared absorbance and Drude–Zener theory.<sup>37,38</sup> A series of control experiments were performed to determine the response of this SnO<sub>x</sub> ALD film to well-defined O<sub>2</sub>, O<sub>2</sub> + CO, and CO gas pressures. The experimental results were then compared with the predictions from the ionosorption and oxygen-vacancy models for semiconductor metal oxide gas sensors.

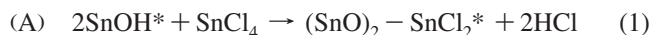
## II. Experimental

The experiments were performed in a viscous-flow ALD reactor specially designed for in situ transmission FTIR studies.<sup>25,39,40</sup> Briefly, the core of the reactor was a four-way cross with 2.75 in Conflat flanges. The entry lines for the reactants and gases were on the front port. Two 1 cm thick CsI salt windows allowed the IR beam to be transmitted through

the reactor. Gate valves protected the CsI windows from deposition. A standard six-way cross was connected on the back port. The six-way cross connected to a capacitance manometer for pressure measurements and an Alcatel 2015 mechanical vacuum pump. A sample holder and electrical and thermocouple feedthroughs also connected at the six-way cross. The temperature of the reactor was maintained at 200 °C by a ceramic heater that could be controlled with an accuracy of 0.05 °C.

The substrate was prepared by pressing SiO<sub>2</sub> nanoparticles into tungsten mesh using a stainless-steel die.<sup>29,41,42</sup> The SiO<sub>2</sub> powders were from Aldrich and had an average diameter of 14 nm. The tungsten mesh was from Buckbee Mears Co. and had a spacing of 100 lines/inch and a light transmission of approximately 50%. The substrate had dimensions of 2 cm × 3 cm and a thickness of 50 μm. The SiO<sub>2</sub> nanoparticles had a very high surface area that is necessary for transmission FTIR studies.<sup>29,41,42</sup> In addition to holding the particles, the tungsten grid was used as an electrical heater. A K-type thermocouple was attached on the tungsten mesh. The temperature of the substrate could be controlled accurately using a SIMSPEC 101B temperature controller.

The tin oxide films were deposited on the SiO<sub>2</sub> nanoparticles at 325 °C using ALD techniques. The reactants in the tin oxide ALD process were SnCl<sub>4</sub> and H<sub>2</sub>O<sub>2</sub>.<sup>25,26</sup> The two, sequential, self-limiting surface chemical reactions for tin oxide ALD can be described as



where \* indicates the surface species. Previous investigations have revealed that tin oxide ALD films grown at 325 °C have an oxygen deficiency and are described as SnO<sub>x</sub> where  $x < 2$ .<sup>25</sup> Typical SnO<sub>x</sub> ALD growth rates are ~0.7 Å per AB cycle at 325 °C.<sup>25</sup> Auger and X-ray photoelectron studies are consistent with very understoichiometric films with  $x = 1.1–1.2$  and  $x = 1.4–1.5$ , respectively.<sup>25</sup>

The ALD process was conducted in a sequence as SnCl<sub>4</sub> exposure, N<sub>2</sub> purge and evacuation, H<sub>2</sub>O<sub>2</sub> exposure, and N<sub>2</sub> purge and evacuation. During the reactant exposures, the reactor was closed to the mechanical pump and exposed to the reactants for 60 s. The reactant exposures were  $1.6 \times 10^8$  L (L =  $1 \times 10^{-6}$  Torr·s). These large exposures ensured that the ALD surface reactions reached completion. After the reactant exposures, the chamber was purged with a N<sub>2</sub> gas flow and then evacuated to prevent any chemical vapor deposition. The gate valves between the salt windows and the reactor were opened, and the FTIR spectra were recorded after the N<sub>2</sub> purge and evacuation.

The SnO<sub>x</sub> ALD films were grown using 16 AB cycles at 325 °C. This number of AB cycles produced a background infrared absorbance for the SnO<sub>x</sub> ALD film that was approximately in the middle of the measurable absorbance range. From earlier studies, these 16 AB cycles deposit a SnO<sub>x</sub> ALD film with a thickness of ~10 Å. Following the deposition of the SnO<sub>x</sub> ALD film, the substrate was heated to 350 °C in an oxygen pressure of about 20 Torr for 30 min. Subsequently, the reactor was evacuated, and the substrate was exposed to a fresh oxygen pressure of 20 Torr for 1 h at 300 °C. This pretreatment yielded stable and reproducible SnO<sub>x</sub> ALD films on the SiO<sub>2</sub> nanoparticles as measured by the in situ transmission FTIR spectra.

After the pretreatment, the substrate was ready for the gas sensing studies at 300 °C. The FTIR spectra were recorded under different pressures of O<sub>2</sub>, CO, or both O<sub>2</sub> and CO. These experiments were conducted in either flow or static modes. In

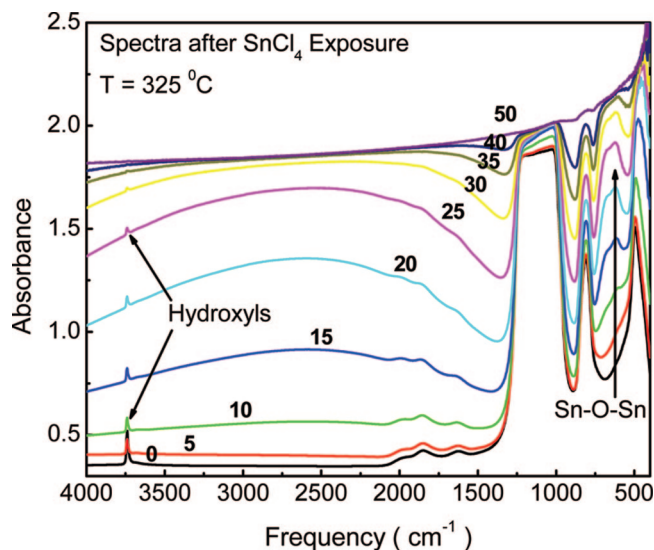


**Figure 2.** Absolute FTIR spectra showing the infrared absorbance after various numbers of AB cycles during  $\text{SnO}_x$  ALD at  $325^\circ\text{C}$ . The spectra were recorded after the  $\text{SnCl}_4$  exposures.

the flow mode, the gas pressures were determined by the flow rates of the mass flow controllers. In the static mode, the gate valve was closed to the mechanical pump, and the gases were trapped in the reactor.

The electrical conductivity of the  $\text{SnO}_x$  ALD films was measured using the background infrared absorbance. This measurement technique eliminates the need to make electrical connections to the substrate. For semiconductor samples, a portion of the infrared absorption results from free charge carriers. According to Drude–Zener theory,<sup>37,38</sup> the absorbance at a given wavelength is directly related to the electrical conductivity according to

$$A(\lambda) = \sigma(\lambda)z/\epsilon_0 A(\lambda) = \sigma(\lambda)z/\epsilon_0 c n c n \quad (3)$$

where  $A(\lambda)$  is the absorbance at the wavelength  $\lambda$ . In addition,  $\sigma(\lambda)$  is the electrical conductivity depending on the wavelength,  $z$  is the thickness of the sample,  $\epsilon_0$  is the permittivity,  $c$  is the light velocity, and  $n$  is the refractive index of the material.

### III. Results and Discussion

#### A. $\text{SnO}_x$ ALD Film Growth and Response to $\text{O}_2$ and $\text{CO}$ .

The  $\text{SnO}_x$  ALD film growth on the  $\text{SiO}_2$  nanoparticles at  $325^\circ\text{C}$  could be monitored using in situ transmission FTIR spectroscopy. FTIR spectra recorded versus the number of AB reaction cycles after the  $\text{SnCl}_4$  exposure are shown in Figure 2. These spectra are similar to the previously reported spectra after the  $\text{H}_2\text{O}_2$  exposures.<sup>25</sup> The FTIR spectra are all presented on the same absolute scale. The FTIR spectrum for the initial  $\text{SiO}_2$  nanoparticles prior to any AB cycles is labeled as 0. This spectrum displays three peaks in the region of  $400\text{--}1300\text{ cm}^{-1}$  that are characteristic of  $\text{SiO}_2$ .<sup>25</sup> There are also combination bands of these peaks that are observed in the region between  $1500\text{--}2200\text{ cm}^{-1}$ . The initial  $\text{SiO}_2$  surface also displays strong O–H stretching vibrations at  $3740\text{ cm}^{-1}$  that help initiate the ALD surface chemistry.

Figure 2 also shows spectra during 50 AB cycles of  $\text{SnO}_x$  ALD. The main absorbance change during these 50 AB cycles is the increasing background infrared absorbance. During  $\text{SnO}_x$  ALD, infrared absorbance at  $600\text{--}690\text{ cm}^{-1}$  also grew progressively with the number of AB cycles. This infrared absorbance results from the bulk  $\text{SnO}_x$  vibrational modes.<sup>25,43,44</sup> During the

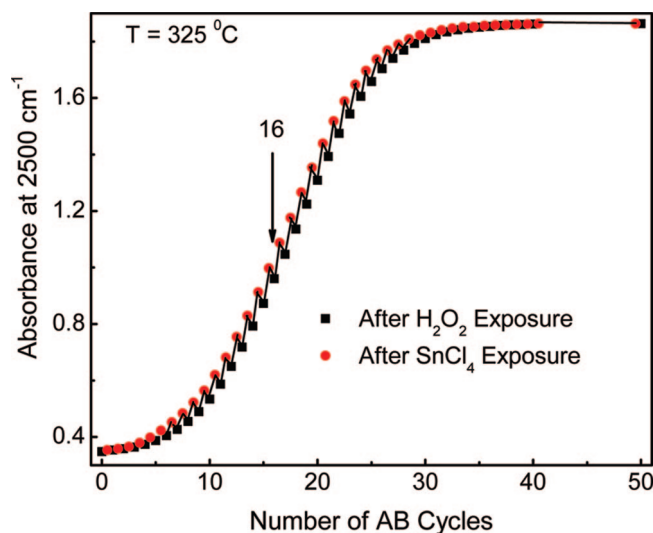


**Figure 3.** Infrared absorbance at  $2500\text{ cm}^{-1}$  after each  $\text{SnCl}_4$  and  $\text{H}_2\text{O}_2$  exposure during the AB cycles for  $\text{SnO}_x$  ALD at  $325^\circ\text{C}$ . The gas sensing experiments were performed after 16 AB cycles.

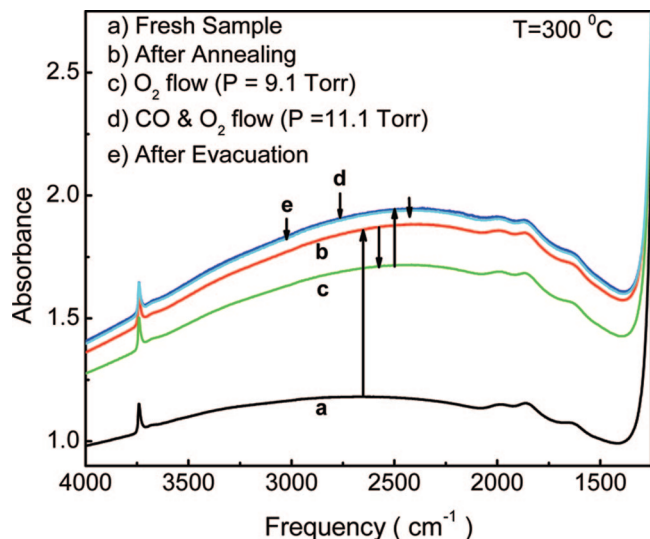
sequential surface reactions, the O–H stretching vibrations from  $\text{SnO}\text{--H}$  surface species appeared after the  $\text{H}_2\text{O}_2$  exposures and were extinguished after the  $\text{SnCl}_4$  exposures.<sup>25</sup> The Sn–Cl stretching vibrations that would have been observed at  $\sim 360\text{--}380\text{ cm}^{-1}$  after the  $\text{SnCl}_4$  exposures were masked by the strong  $\text{SiO}_2$  bulk modes.

Figure 3 displays the increase of the background infrared absorbance at  $2500\text{ cm}^{-1}$  versus the number of AB cycles at  $325^\circ\text{C}$ . A similar increase in background absorbance was observed earlier and attributed to the electrical conductivity of the  $\text{SnO}_x$  ALD film.<sup>25</sup> There is only a small increase during the first five AB cycles. This small initial growth indicates a short nucleation period for the  $\text{SnO}_x$  ALD films. After the initial nucleation period, the absorbance increases progressively and is consistent with the linear growth of the  $\text{SnO}_x$  ALD films. A close examination of the results in Figure 3 reveals that the exposure to  $\text{SnCl}_4$  results in an increase of the background absorbance. In contrast, the exposure to  $\text{H}_2\text{O}_2$  results in a smaller decrease of the background absorbance. This behavior is consistent with the increase and decrease of the free charge carriers in the  $\text{SnO}_x$  ALD film by the added  $\text{--SnCl}_2^*$  and  $\text{--OH}^*$  surface species, respectively.

The background absorbance increases more slowly after 25 AB cycles and then asymptotically levels off after 35 AB cycles. As discussed earlier, this limiting of the background infrared absorbance is caused by pinholes in the tungsten mesh sample.<sup>25</sup> The maximum absorbance indicates that about 2% of the surface area of the tungsten mesh is occupied by pinholes. The linear region of increase in the infrared absorbance occurs between the 10th and the 30th AB cycle. Consequently, the  $\text{SnO}_x$  ALD films used in this gas sensing study were grown by using 16 AB cycles. These  $\text{SnO}_x$  ALD films yield an infrared absorbance that is approximately in the middle of the region of linear absorbance growth with number of AB cycles as shown in Figure 3.

The thickness of the  $\text{SnO}_x$  ALD films grown using 16 AB cycles should be  $\sim 10\text{ \AA}$ . This estimate is based on a growth of  $\sim 0.7\text{ \AA}$  per AB cycle obtained by previous quartz crystal microbalance measurements.<sup>25</sup> In addition, this estimate assumes a short nucleation period. The  $\text{SnO}_x$  ALD film thickness of  $\sim 10\text{ \AA}$  is less than the Debye length for tin oxide. Previous studies have reported that the Debye length for an ultrathin particle





**Figure 4.** Absolute FTIR spectra (a) for freshly prepared  $\text{SnO}_x$  ALD sample, (b) after thermal annealing pretreatment, (c) for an  $\text{O}_2$  flow yielding an  $\text{O}_2$  pressure of 9.1 Torr, (d) for an  $\text{O}_2$  flow yielding an  $\text{O}_2$  pressure of 9.1 Torr and a CO flow yielding a pressure of 2.0 Torr, and (e) after evacuation of both the  $\text{O}_2$  and CO flows.

film of  $\text{SnO}_2$  was 30.6 Å at 250 °C.<sup>17</sup> By using the same parameters as those given in ref 17, the calculated Debye lengths in  $\text{SnO}_2$  at 300 and 325 °C are 32.0 and 32.7 Å, respectively. Recent measurements of the sensor response of the  $\text{SnO}_x$  ALD films versus film thickness at 300 °C also were consistent with a Debye length of ~26 Å.<sup>12</sup> Because the film thickness is less than the Debye length, the electrical conductivity of these  $\text{SnO}_x$  ALD films should be modulated dramatically by oxygen vacancies or ionosorbed oxygen species on the surface of the  $\text{SnO}_x$  ALD film.

Figure 4 shows FTIR absorption spectra that reveal the general trends during the pretreatment of the  $\text{SnO}_x$  ALD films and their response to  $\text{O}_2$  and CO pressure. All these FTIR spectra were recorded at 300 °C. Curve a in Figure 4 shows the spectrum of a freshly prepared  $\text{SnO}_x$  ALD sample with characteristic O–H stretching vibrations resulting from  $\text{SnOH}^*$  surface species. Curve b in Figure 4 then shows the spectrum after the annealing pretreatment. The background absorbance increases greatly in going from curve a to curve b in Figure 4. This increase in infrared absorbance is consistent with the loss of oxygen from the ultrathin  $\text{SnO}_x$  ALD film with a thickness of 10 Å during thermal annealing that results in oxygen vacancies.<sup>45</sup> According to the oxygen-vacancy model, the oxygen vacancies can ionize to produce electrons in the conduction band of the  $\text{SnO}_x$  ALD film.<sup>8</sup> These conduction electrons increase the electrical conductivity and the infrared absorbance according to Drude–Zener theory.<sup>37,38</sup>

The  $\text{SnO}_x$  ALD film is then exposed to an  $\text{O}_2$  flow that produces an  $\text{O}_2$  pressure of  $P_{\text{O}_2} = 9.1$  Torr in the reactor. Curve c in Figure 4 shows the spectrum of the sample with an  $\text{O}_2$  pressure of 9.1 Torr. The background infrared absorbance decreases greatly compared with the background infrared absorbance after thermal annealing. This decrease is attributed to the ability of  $\text{O}_2$  to fill oxygen vacancies and recapture the free electron charge carriers from the  $\text{SnO}_x$  ALD film. This recapture of the free electron charge carriers lowers the electrical conductivity and the background absorbance. Alternatively, the decrease could result from ionosorbed oxygen species on the  $\text{SnO}_x$  ALD film surface that capture free electron charge carriers from the bulk of the  $\text{SnO}_x$  ALD film. The loss of these free electrons

from the bulk decreases the electrical conductivity and lowers the background infrared absorbance. There is no indication in the FTIR spectrum in curve c in Figure 4 of the ionosorbed oxygen species ( $\text{O}_2^-$ ,  $\text{O}^-$ , or  $\text{O}^{2-}$ ) on the surface of the  $\text{SnO}_x$  ALD film. However, these ionosorbed oxygen species may be present at a coverage that is too low to be detected in the FTIR absorption spectrum.

Curve d in Figure 4 then shows the spectrum after CO was added to increase the pressure to 11.1 Torr. The background infrared absorbance shows a pronounced increase with the addition of CO pressure. A similar increase in the background infrared absorbance upon CO addition was observed earlier by Baraton and co-workers.<sup>19,33,37,46</sup> This increase is attributed to the ability of CO to react with surface oxygen species to produce  $\text{CO}_2$ . The loss of surface oxygen species may produce new oxygen vacancies that will subsequently ionize and add electron charge carriers to the bulk of the  $\text{SnO}_x$  ALD film. Alternatively, the CO may react with ionosorbed oxygen species to produce  $\text{CO}_2$ . The electrons then return to the  $\text{SnO}_x$  ALD film as free charge carriers. The increase in electron charge carriers increases the electrical conductivity and the background infrared absorbance.

Finally, curve e in Figure 4 displays the spectrum after evacuating the reactor. After evacuation, the background infrared absorbance does not return to the initial background absorbance after the thermal annealing pretreatment shown in curve b in Figure 4. Some changes have occurred in the  $\text{SnO}_x$  ALD film after the initial gas exposures. However, the subsequent response of this  $\text{SnO}_x$  ALD film was very reproducible. Multiple exposures to  $\text{O}_2$  and then to CO and  $\text{O}_2$  yielded consistent results and indicated that the  $\text{SnO}_x$  ALD film was stable.

**B.  $\text{O}_2$  and CO Gas Sensing Using Flow Conditions.** The FTIR spectra were examined carefully as a function of  $\text{O}_2$  and CO pressure under gas-flow conditions. These experiments were performed to attempt to observe any surface species and to quantify the change in the background infrared absorbance versus  $\text{O}_2$  and CO pressure. Figure 5a shows FTIR spectra versus a range of  $\text{O}_2$  pressures at 300 °C. As expected from the results shown in Figure 4, the  $\text{O}_2$  pressures cause a decrease in the background infrared absorbance. The change in background infrared absorbance occurs rapidly with increasing  $\text{O}_2$  pressure. The background infrared absorbance at 2500  $\text{cm}^{-1}$  versus  $\text{O}_2$  pressure is shown in Figure 5b. Most of the change in the background infrared absorbance occurs by an  $\text{O}_2$  pressure of only 0.24 Torr.

The decreasing background infrared absorbance is consistent with a decrease of the electrical conductivity of the  $\text{SnO}_x$  ALD film. The decreasing electrical conductivity is caused by the loss of free electron charge carriers in the  $\text{SnO}_x$  ALD film. The electron charge carriers are removed as  $\text{O}_2$  refills oxygen vacancies on the surface of the  $\text{SnO}_x$  ALD film or  $\text{O}_2$  binds on the surface as ionosorbed species. The changes observed versus  $\text{O}_2$  pressure are consistent with both models and cannot be used to distinguish between the oxygen-vacancy or ionosorption models.

The FTIR spectra in Figure 5a also do not show any additional spectral features between 1300–4000  $\text{cm}^{-1}$  that may be consistent with ionosorbed oxygen species. However, the vibrational frequencies of these oxygen species may be obscured by the infrared absorption of the  $\text{SiO}_2$  nanoparticles. The infrared absorption of  $\text{O}_2^-$  and  $\text{O}_2^{2-}$  are expected at vibrational frequencies of 1145 and 842  $\text{cm}^{-1}$ , respectively.<sup>47</sup> These vibrational frequencies are for  $\text{O}_2$  in  $\text{KO}_2$  and  $\text{Na}_2\text{O}_2$ , respectively.<sup>47</sup> Depending on the coordination geometry,  $\text{O}_2$  should also display vibrational frequencies of 1075–1300  $\text{cm}^{-1}$  for the bent end-

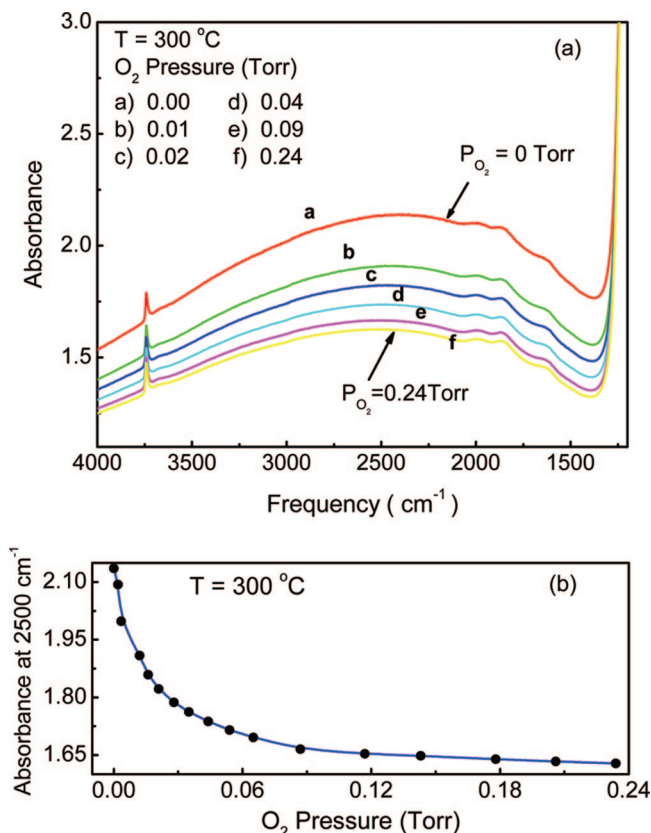


**Figure 5.** (a) Absolute FTIR spectra and (b) background infrared absorbance at  $2500\text{ cm}^{-1}$  versus  $\text{O}_2$  pressure at  $300\text{ }^{\circ}\text{C}$ .

on superoxo species and  $790\text{--}985\text{ cm}^{-1}$  for the symmetrical side-on peroxy species.<sup>7,48</sup>

Although the  $\text{SiO}_2$  nanoparticles may prevent the observation of ionosorbed oxygen species in this study, the existence of these species has recently been subject to debate. Gurlo has argued that previous spectroscopic studies have not been able to identify ionosorbed oxygen species under working conditions for metal oxide gas sensors.<sup>7,8</sup> In order for this study to add to this debate, the current experiments would need to be repeated on an underlying particle support that did not absorb strongly in the infrared spectral region between  $800\text{--}1300\text{ cm}^{-1}$ . The  $\text{O}_2$  pressures of  $<0.24\text{ Torr}$  examined in Figure 5 are also much lower than the typical working conditions for metal oxide gas sensors at atmospheric pressure. The ionosorbed oxygen species may not be present at these low  $\text{O}_2$  pressures.

The  $\text{SnO}_x$  ALD film was then exposed to  $\text{O}_2$  and varying CO pressures at  $300\text{ }^{\circ}\text{C}$ . These experiments monitored the changes in the background infrared absorption when CO reacted to produce  $\text{CO}_2$  on the surface of the  $\text{SnO}_x$  ALD film. In addition, these experiments attempted to observe any new surface species associated with the CO reaction. The FTIR spectra for an  $\text{O}_2$  pressure of  $3.02\text{ Torr}$  with varying CO pressures are shown in Figure 6a. The  $\text{O}_2$  pressure is lower than typical for working metal oxide gas sensors. However, this  $\text{O}_2$  pressure is large compared with the  $\text{O}_2$  pressure of  $>0.10\text{ Torr}$  needed for  $\text{O}_2$  to reach its saturation response on the  $\text{SnO}_x$  ALD film as shown in Figure 5. These model studies are intended to understand the basic mechanism of the gas sensing response by the  $\text{SnO}_x$  ALD film.

The main change in the FTIR spectra is the increase in the background infrared absorbance with increasing CO pressures. The increase in the background infrared absorbance at  $2500\text{ cm}^{-1}$  versus CO pressure is shown in Figure 6b. The increase

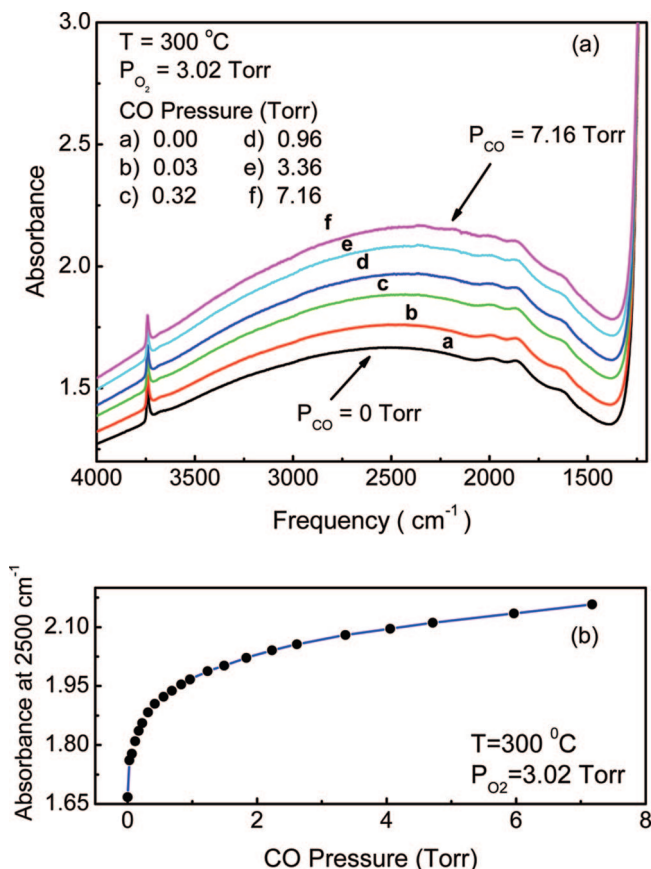


**Figure 6.** (a) Absolute FTIR spectra and (b) background infrared absorbance at  $2500\text{ cm}^{-1}$  versus CO pressure at  $300\text{ }^{\circ}\text{C}$ . The  $\text{O}_2$  pressure was fixed at  $3.02\text{ Torr}$ .

in background infrared absorbance is consistent with the return of free electron charge carriers to the  $\text{SnO}_x$  ALD film. These electron charge carriers increase as a result of CO reacting with surface oxygen and producing new oxygen vacancies or CO reacting with ionosorbed oxygen species. Either reaction would release electrons back to the bulk of the  $\text{SnO}_x$  ALD film. The free electron charge carriers increase the electrical conductivity and infrared absorbance of the  $\text{SnO}_x$  ALD film.

The FTIR spectra also did not monitor any new surface species at any of the CO pressures. Previous studies have detected carbonate species on  $\text{SnO}_2$  particle surfaces at  $300\text{ }^{\circ}\text{C}$  with an  $\text{O}_2$  pressure of  $37.5\text{ Torr}$  and a CO pressure of  $7.5\text{ Torr}$ .<sup>33</sup> This carbonate species was observed at vibrational frequencies of  $1300\text{--}1400\text{ cm}^{-1}$ .<sup>33</sup> The carbonate species were not stable on the  $\text{SnO}_2$  surface and were not observed after the evacuation of  $\text{O}_2$  and CO pressure.<sup>33</sup> The vibrational frequencies for the carbonate species are below the range of frequencies that can be easily observed on the  $\text{SiO}_2$  nanoparticles. In addition, the carbonate species may not have been present at the low  $\text{O}_2$  pressures used in this study.

**C. Observation of Gas Phase  $\text{CO}_2$  Reaction Products Using Static Conditions.** Static experiments were performed to monitor the FTIR spectral changes and pressure during CO gas sensing at  $300\text{ }^{\circ}\text{C}$ . The reactor was first evacuated and the gate valve was then closed between the reactor and the mechanical pump. Subsequently,  $\text{O}_2$  was dosed into the reactor to produce an  $\text{O}_2$  pressure of  $5.26\text{ Torr}$ . Curve a in Figure 7 shows the FTIR spectrum for the substrate exposed to  $5.26\text{ Torr}$  under these static conditions. This FTIR spectrum is similar to spectrum f shown in Figure 5a, except that the absorbance scale has been magnified to observe the various absorbance features.

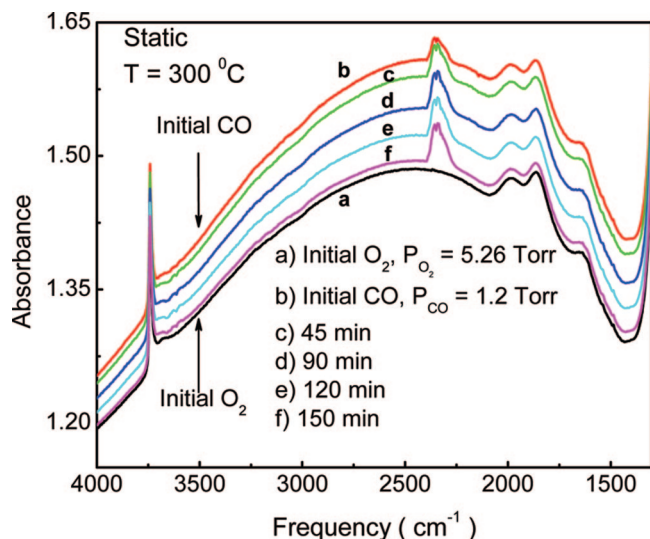


**Figure 7.** Absolute FTIR spectra under static conditions for an initial O<sub>2</sub> pressure of 5.26 Torr followed by an initial CO pressure of 1.2 Torr. The time evolution is then monitored during the reaction of CO with surface oxygen to produce CO<sub>2</sub>.

CO was then dosed into the reactor to produce a CO pressure of 1.2 Torr. Subsequently, FTIR spectra were recorded to capture the spectral changes as CO progressively reacted with oxygen species on the SnO<sub>x</sub> ALD film. The initial FTIR spectrum recorded 15 min after the CO introduction is shown in curve b in Figure 7. The background infrared absorbance increases with the introduction of CO to the reactor. This increase is consistent with the results in Figure 6a and indicates that CO has reacted with surface oxygen species to produce CO<sub>2</sub>. The electrons associated with the oxygen vacancies or the ionosorbed oxygen species then return to the bulk of the SnO<sub>x</sub> ALD film to increase the electrical conductivity and the background infrared absorbance.

Under the static conditions, the CO<sub>2</sub> reaction product builds up in the reactor. The characteristic peaks of CO<sub>2</sub> are observed in Figure 7 by the broad overlapping peaks at ~2340 and ~2360 cm<sup>-1</sup>. These are the broadened P- and R-rotational branches of the CO<sub>2</sub> asymmetric stretching vibration.<sup>49</sup> The rotational structure of these CO<sub>2</sub> peaks is not observed because the FTIR spectra were recorded at a resolution of 4 cm<sup>-1</sup>. The vibrational absorption from CO at ~2145 cm<sup>-1</sup> is also monitored at early times as a very weak peak in curve b in Figure 7. However, the CO absorbance is barely above the noise limit and is not observed at later times.

Curves c–f in Figure 7 show the FTIR spectra recorded at various time intervals after the CO introduction. The absorbance for the CO<sub>2</sub> vibrational peaks increases as the background infrared absorption decreases. These results demonstrate the transient effect of the CO pressure on the background infrared absorption. When CO is available to react with surface oxygen to produce CO<sub>2</sub>, the background absorbance is higher because electron carriers are returned to the bulk of the SnO<sub>x</sub> ALD film. However, the background absorbance decreases when the CO is depleted, resulting from the reaction to produce CO<sub>2</sub>. O<sub>2</sub> can then refill oxygen vacancies or produce O<sub>2</sub> ionosorption species on the surface of the SnO<sub>x</sub> ALD film. This surface oxygen traps electron free carriers and decreases the electrical conductivity and infrared absorbance of the SnO<sub>x</sub> ALD film.

The absorbance of the CO<sub>2</sub> vibrational features is proportional to the CO<sub>2</sub> concentration through the Beer–Lambert law expression,  $I/I_0 = 10^{-A}$ , where  $I$  is the transmitted light intensity,

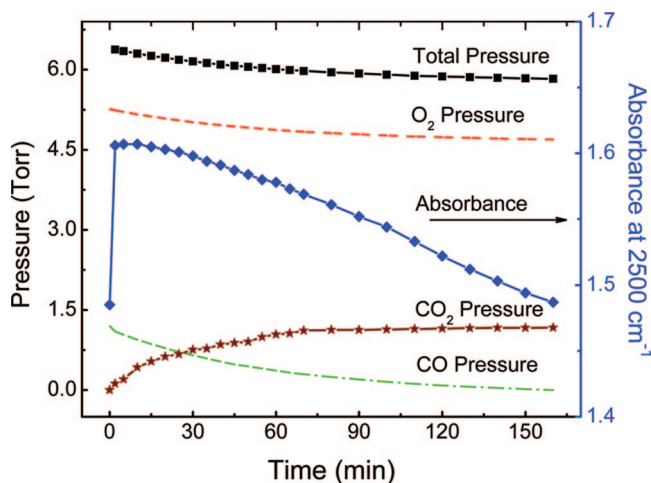


**Figure 8.** Pressures and background infrared absorbance versus time for an initial O<sub>2</sub> pressure of 5.26 Torr followed by an initial CO pressure of 1.2 Torr. The CO<sub>2</sub> pressure is measured by using the integrated absorbance for the CO<sub>2</sub> asymmetric stretching vibration.

$I_0$  is the initial light intensity, and  $A$  is the absorbance,  $A = \epsilon cl$ . In the absorbance expression,  $\epsilon$  is the extinction coefficient,  $c$  is the concentration or pressure, and  $l$  is the path length. The CO<sub>2</sub> pressure in the reactor was obtained by a calibration between the integrated absorbance of the CO<sub>2</sub> asymmetric stretching vibration and CO<sub>2</sub> pressure. This calibration was conducted by introducing known CO<sub>2</sub> pressures into the reactor at 200 °C and then measuring the integrated absorbance of the CO<sub>2</sub> asymmetric stretching vibration from 2210 to 2395 cm<sup>-1</sup>. The integrated absorbance was approximately linear with the CO<sub>2</sub> pressure over the measured range of CO<sub>2</sub> pressures from 0.15 to 1.70 Torr. The CO<sub>2</sub> pressures obtained from the integrated absorbances for the CO<sub>2</sub> asymmetric stretching vibration in Figure 7 and additional FTIR spectra recorded at other times are shown in Figure 8.

The evolution of all the gas pressures can be determined based on the initial O<sub>2</sub> and CO pressures, the total pressure versus time, and the CO<sub>2</sub> pressure obtained from the infrared absorbance for the CO<sub>2</sub> asymmetric stretching vibration. The determination of the O<sub>2</sub> and CO pressures assumes that CO reacts with surface oxygen species from O<sub>2</sub> to produce CO<sub>2</sub>. Figure 8 shows all the pressures versus time after the CO introduction. The O<sub>2</sub>, CO, and total pressures and the background infrared absorbance all decrease versus time. In contrast, the CO<sub>2</sub> pressure increases versus time. The O<sub>2</sub> pressure is large enough that sufficient O<sub>2</sub> remains after the depletion of CO to reduce the background infrared absorbance.

#### D. Detecting CO Without O<sub>2</sub> Using Flow Conditions.

Additional experiments were performed by exposing CO to the SnO<sub>x</sub> ALD film in the absence of O<sub>2</sub> to measure the change in background infrared absorbance and to determine whether CO gas pressure alone produced any new surface species. Prior to these experiments, the chamber was purged for 1 h at 300 °C to remove any remaining residual gas species. Subsequently, CO was flowed into the reactor, and FTIR spectra were recorded at various CO pressures. The FTIR spectra in Figure 9a reveal that CO pressure dramatically increases the background infrared absorbance at very low CO pressures. In addition, no new surface species are observed in the frequency range from 1300 to 4000 cm<sup>-1</sup>.

A summary of the change in the background infrared absorbance versus CO pressure in the absence of O<sub>2</sub> is shown in Figure 9b. The increase in the background infrared absorbance



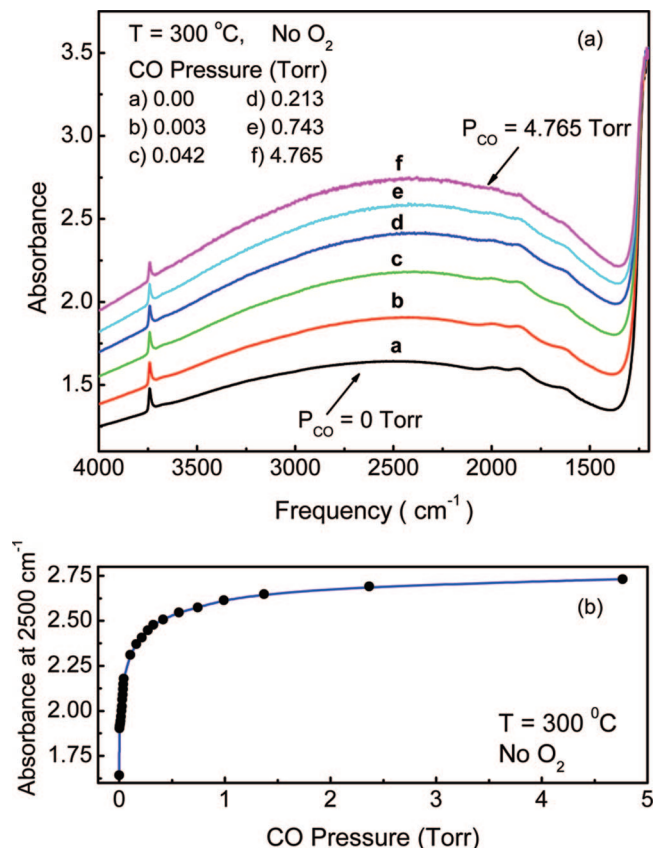


**Figure 9.** (a) Absolute FTIR spectra and (b) background infrared absorbance at 2500  $\text{cm}^{-1}$  versus CO pressure in the absence of  $\text{O}_2$  pressure at 300 °C.

is noticeably larger than the increase observed with CO pressure in the presence of  $\text{O}_2$  pressure shown in Figure 6. This larger absorbance is consistent with more oxygen vacancies or chemisorbed CO in the absence of  $\text{O}_2$  pressure. CO can react with surface oxygen atoms to produce  $\text{CO}_2$  and create an oxygen vacancy. The oxygen vacancies can then ionize and donate their electrons to the conduction band of the  $\text{SnO}_x$  ALD film. If  $\text{O}_2$  is not present to refill the oxygen vacancies, the electrical conductivity can remain very high. In addition, CO may chemisorb and produce  $\text{CO}^+$  species that may yield additional electrons as free carriers in the  $\text{SnO}_x$  ALD film.<sup>8</sup>

These results call into question the generally accepted ionosorption model for semiconductor metal oxide sensors and the necessity of  $\text{O}_2$  for sensor operation. Earlier experiments also observed that  $\text{SnO}_2$  films could detect CO at 200–400 °C at very low  $\text{O}_2$  concentrations.<sup>50</sup> More recent experiments also measured a large response for  $\text{SnO}_2$  sensors to CO in the absence of  $\text{O}_2$ .<sup>51</sup>  $\text{O}_2$  may be necessary to return the conductivity of the  $\text{SnO}_2$  sensor to its initial value prior to CO exposures. However,  $\text{SnO}_2$  sensors can respond very sensitively to CO pressure without concurrent  $\text{O}_2$  exposures.

#### E. Transient Behavior During $\text{O}_2$ and CO Gas Sensing.

The last set of experiments was performed to examine the time scale of the response of the  $\text{SnO}_x$  ALD films. These investigations were performed using flow experiments. Figure 10 shows the background infrared absorbance versus time during introduction and evacuation of  $\text{O}_2$  from the reactor at 300 °C. The  $\text{O}_2$  pressure introduced into the reactor was 11.9 Torr. Figure 10 reveals that the absorbance decreases rapidly over 100–200 s when the  $\text{O}_2$  pressure is added to the reactor. The absorbance decrease then gradually slows and asymptotically limits for times after  $\text{O}_2$  introduction longer than 800 s.

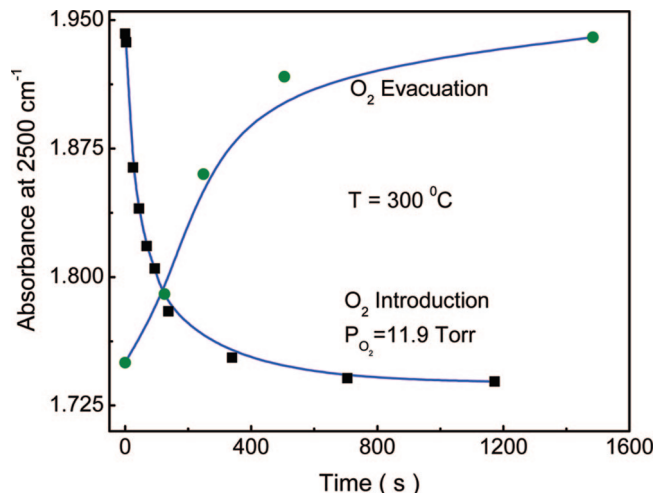


**Figure 10.** Background infrared absorbance at 2500  $\text{cm}^{-1}$  versus time during  $\text{O}_2$  introduction and  $\text{O}_2$  evacuation at 300 °C. The  $\text{O}_2$  pressure during introduction was 11.9 Torr.

The different time scales observed in Figure 10 indicate that different processes affect the transient response of the  $\text{SnO}_x$  ALD film. The rapid response is attributed to  $\text{O}_2$  filling oxygen vacancies on the surface of the  $\text{SnO}_x$  ALD film or  $\text{O}_2$  adsorbing onto the  $\text{SnO}_x$  ALD film to create ionosorbed  $\text{O}_2$  species. The longer time response is explained by oxygen atoms more slowly diffusing into the  $\text{SnO}_x$  ALD film to fill oxygen vacancies in the bulk of the film. The diffusion times can be much longer than the adsorption times even though the ultrathin  $\text{SnO}_x$  films have thicknesses of only  $\sim 10$  Å.

Figure 10 also shows the transient results for  $\text{O}_2$  evacuation from the reactor. The background infrared absorbance increases rapidly over 200–300 s when  $\text{O}_2$  pressure is removed from the reactor. The absorbance increase then gradually slows and asymptotically limits for times after  $\text{O}_2$  removal longer than 800 s. The time scale for these absorbance changes is very similar to the time scale for the absorbance changes during  $\text{O}_2$  introduction. The magnitude of the changes during  $\text{O}_2$  introduction and evacuation is also identical and reveals that the effect of  $\text{O}_2$  is reversible.

Similar experiments were also performed to investigate the transient results for CO introduction and evacuation in the presence of  $\text{O}_2$ . Figure 11a shows the background infrared absorbance change during CO introduction at a pressure of 2.5 Torr. The initial  $\text{O}_2$  pressure was 4.2 Torr. The introduction of the CO pressure causes a rapid increase in the background infrared absorbance in only 10–20 s. Figure 11b shows the background infrared absorbance change during CO evacuation with the same  $\text{O}_2$  pressure. The background infrared absorbance decreases versus time over the same magnitude as that of the increase in Figure 11a. However, the time scale for the decrease during CO evacuation is much larger than the time scale for the increase during CO introduction.

The different time scales observed in Figure 11a,b reflect the different kinetics for either the CO reaction with surface oxygen to produce  $\text{CO}_2$  or  $\text{O}_2$  refilling oxygen vacancies or forming ionosorption species on the surface of the  $\text{SnO}_x$  ALD film. The rapid absorbance change observed in Figure 11a argues that the CO reaction with surface oxygen to produce  $\text{CO}_2$  is a fast process. In contrast, the slower absorbance change monitored in Figure 11b indicates that  $\text{O}_2$  refilling oxygen vacancies or forming ionosorption species requires additional time. The adsorption of  $\text{O}_2$  to form ionosorption species is an adsorption process and would be expected to occur on a much shorter time

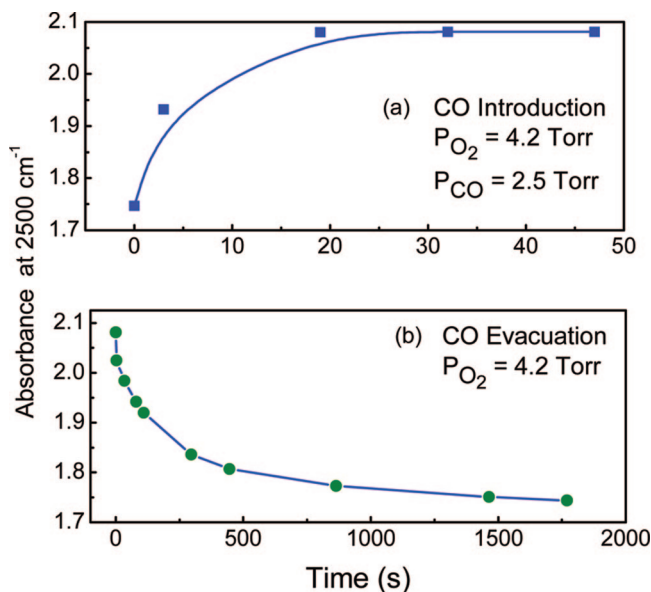


**Figure 11.** Background infrared absorbance at 2500 cm<sup>-1</sup> versus time during CO introduction and CO evacuation at 300 °C. The O<sub>2</sub> pressure was 4.2 Torr. The CO pressure during introduction was 2.5 Torr.

scale. Consequently, the longer time scale in Figure 11b suggests that this transient behavior is dominated by O<sub>2</sub> refilling oxygen vacancies.

The time scale of the transient behavior during exposure to O<sub>2</sub> and CO have also been reported for SnO<sub>2</sub> nanopowders with diameters of 8 and 14 nm.<sup>37</sup> The infrared transmission by the SnO<sub>2</sub> nanopowders was measured during CO addition, CO evacuation, and O<sub>2</sub> addition. These earlier experiments were qualitatively consistent with the results of the current studies. Transient responses were observed in ~10 min or ~600 s following the CO addition, CO evacuation, and O<sub>2</sub> addition.<sup>37</sup> The slightly longer response times may have resulted from the larger SnO<sub>2</sub> grain sizes. However, the time resolution of these earlier experiments was low, and more rapid responses may have been observed at higher time resolution.

Experiments were also performed to investigate the transient results for CO introduction and evacuation in the absence of O<sub>2</sub>. For these experiments, the reactor was initially exposed to O<sub>2</sub> to fill oxygen vacancies and obtain a characteristic SnO<sub>x</sub> ALD film prior to CO reaction. The O<sub>2</sub> was evacuated and then CO was introduced into the reactor and FTIR spectra were recorded versus time. The background infrared absorbance versus time for CO introduction without O<sub>2</sub> is shown in Figure 12. The absorbance increases with time as expected given the previous results in Figure 9. The absorbance increase is rapid and reaches a limiting value in ~200 s.

The CO was then evacuated from the reactor and FTIR spectra were recorded to monitor the transient behavior in the absence of O<sub>2</sub>. Figure 12 shows that the background infrared absorbance decreases versus time after CO evacuation. The time scale for the decrease is similar to the time scale for the increase during CO introduction. However, the magnitude of the decrease is much less than the magnitude of the increase during CO introduction. This behavior argues that CO introduction produces both reversible and irreversible effects on the SnO<sub>x</sub> ALD film.

The increase in the background infrared absorbance with CO introduction is consistent with CO reacting with surface oxygen to produce oxygen vacancies or CO adsorbing as CO<sup>+</sup>. Both of these processes would donate electrons to the conduction band of the SnO<sub>x</sub> ALD film and increase the electrical

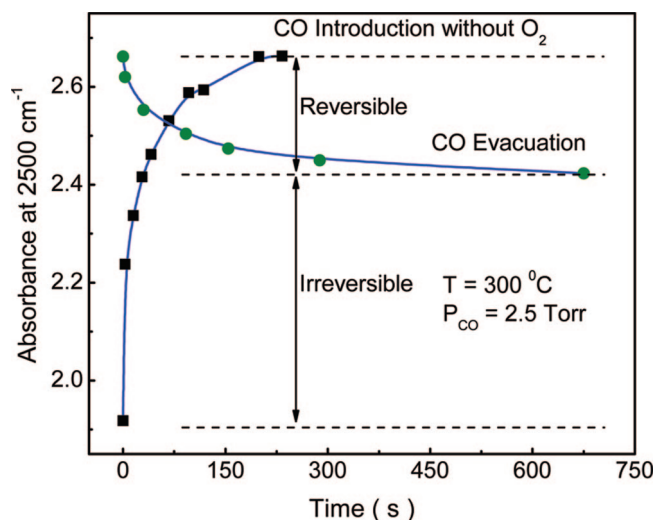


**Figure 12.** Background infrared absorbance at 2500 cm<sup>-1</sup> versus time during CO introduction and CO evacuation without O<sub>2</sub> at 300 °C. The CO pressure during introduction was 2.5 Torr.

conductivity. Figure 12 shows that the decrease of the absorbance with CO evacuation does not return the absorbance to its initial value prior to CO introduction. This smaller absorbance decrease is attributed to the irreversible reaction of CO with surface oxygen that produces oxygen vacancies. These vacancies remain after CO evacuation and will not be filled until O<sub>2</sub> is reexposed to the SnO<sub>x</sub> ALD film. This portion of the absorbance change is labeled as irreversible in Figure 12.

In contrast, the CO chemisorbing as CO<sup>+</sup> and donating an electron to the conduction band of the SnO<sub>x</sub> ALD film would be a reversible process. After the CO evacuation, the chemisorbed CO species could desorb and lower the free electrons in the conduction band of the SnO<sub>x</sub> ALD film. The CO desorption would then lower the background infrared absorbance. This portion of the absorbance change is labeled as reversible in Figure 12. The relative fractions of irreversible and reversible absorbance help quantify the relative importance of CO reaction to produce oxygen vacancies and CO adsorption to yield CO<sup>+</sup> chemisorbed species.

#### IV. Conclusions

Tin oxide ultrathin films were deposited on SiO<sub>2</sub> nanoparticles using ALD techniques at 325 °C. Following an annealing pretreatment, the SnO<sub>x</sub> ALD films with a thickness of ~10 Å were exposed to O<sub>2</sub> and CO gas at 300 °C. The electrical conductivity of the SnO<sub>x</sub> ALD films was measured using in situ transmission FTIR spectroscopy. FTIR spectroscopy can monitor the electrical conductivity of the SnO<sub>x</sub> ALD films because the background infrared absorbance is proportional to the electrical conductivity according to Drude–Zener theory. FTIR spectroscopy can also detect gas-phase species and surface species on the SnO<sub>x</sub> ALD film.

The O<sub>2</sub> pressures were observed to decrease the SnO<sub>x</sub> film conductivity. This decrease was consistent with the filling of oxygen vacancies in the oxygen-vacancy model or the adsorption of ionosorbed oxygen species on the surface of the SnO<sub>x</sub> film in the ionosorption model. Both of these processes would remove electron charge carriers from the bulk of the SnO<sub>x</sub> film and lower the electrical conductivity and background infrared absorbance. Addition of CO then increased the SnO<sub>x</sub> film conductivity. This increase was consistent with CO reacting with surface oxygen to produce oxygen vacancies or reacting with



ionisorbed oxygen species. Both of these processes would return electron charge carriers to the bulk of the  $\text{SnO}_x$  film and increase the electrical conductivity and background infrared absorbance.

Static experiments observed the increase of gas-phase  $\text{CO}_2$  reaction products as the CO reacted with surface oxygen species. Other experiments showed that CO could be easily detected in the absence of  $\text{O}_2$  pressure. The background infrared absorbance increased with CO exposure in the absence of  $\text{O}_2$ . These results suggested that CO can produce oxygen vacancies on the  $\text{SnO}_x$  surface that ionize and release electrons that increase the  $\text{SnO}_x$  film conductivity as suggested by the oxygen-vacancy model. In addition, CO may chemisorb to the surface of the  $\text{SnO}_x$  film as  $\text{CO}^+$  ion and donate an electron to the conduction band of the  $\text{SnO}_x$  film. CO evacuation in the absence of  $\text{O}_2$  also did not return the  $\text{SnO}_x$  film conductivity to its original value prior to the CO exposure. As expected from the oxygen-vacancy model, the film conductivity cannot return to its original value until  $\text{O}_2$  is available to refill the oxygen vacancy.

The transient behavior of the  $\text{SnO}_x$  films to  $\text{O}_2$  and CO was determined by measuring the FTIR spectra versus time. The  $\text{SnO}_x$  films responded to  $\text{O}_2$  introduction and evacuation reversibly within  $\sim 100$  s. The  $\text{SnO}_x$  films responded to CO introduction and evacuation reversibly in the presence of  $\text{O}_2$ . However, CO introduction occurred within  $\sim 10$  s, and CO evacuation occurred over a larger time scale of  $\sim 100$  s. This difference was explained by the different kinetics for CO reaction with surface oxygen to produce  $\text{CO}_2$  compared with the kinetics for  $\text{O}_2$  refilling of oxygen vacancies or  $\text{O}_2$  adsorbing on the surface as ionisorbed surface species.

The ultrathin  $\text{SnO}_x$  ALD films on  $\text{SiO}_2$  nanoparticles with thicknesses less than the Debye length have helped clarify the response of semiconductor metal oxide gas sensors to  $\text{O}_2$  and CO. The changes in background infrared absorbance are consistent with the ionosorption and oxygen-vacancy models for chemiresistant semiconductor gas sensors. The results for CO gas sensing in the absence of  $\text{O}_2$  pressure and the transient responses following CO evacuation with and without  $\text{O}_2$  argue for the importance of the oxygen-vacancy model. Conformal and ultrathin  $\text{SnO}_x$  ALD films deposited on other nanoscale supports may help improve the sensitivity, reliability, and response time of semiconductor metal oxide gas sensors.

**Acknowledgment.** This work was supported by the National Science Foundation (CHE-0715552 and CHE-040855).

## References and Notes

- (1) Seiyama, T.; Kato, A.; Fujiishi, K.; Nagatani, M. *Anal. Chem.* **1962**, *34*, 1502.
- (2) Taguchi, N. Japan Patent 45-38200, 1962.
- (3) Wang, C. C.; Akbar, S. A.; Madou, M. J. *J. Electroceram.* **1998**, *2*, 273.
- (4) Williams, D. E. *Sens. Actuators, B* **1999**, *57*, 1.
- (5) Martinelli, G.; Carotta, M. C. *Sens. Actuators, B* **1995**, *23*, 157.
- (6) Barsan, N.; Koziej, D.; Weimar, U. *Sens. Actuators, B* **2007**, *121*, 18.
- (7) Gurlo, A. *ChemPhysChem* **2006**, *7*, 2041.
- (8) Gurlo, A.; Riedel, R. *Angew. Chem., Int. Ed.* **2007**, *46*, 3826.
- (9) Hauffe, K. *Adv. Catal.* **1955**, *7*, 213.
- (10) Morrison, S. R. *Adv. Catal.* **1955**, *7*, 259.
- (11) Zemel, J. N. *Thin Solid Films* **1988**, *163*, 189.
- (12) Du, X.; George, S. M. *Sens. Actuators, B* **2008**, in press.
- (13) Franke, M. E.; Koplin, T. J.; Simon, U. *Small* **2006**, *2*, 36.
- (14) Xu, C.; Tamaki, J.; Miura, N.; Yamazoe, N. *Sens. Actuators, B* **1991**, *3*, 147.
- (15) Yamazoe, N. *Sens. Actuators, B* **1991**, *5*, 7.
- (16) Mizsei, J. *Sens. Actuators, B* **1995**, *23*, 173.
- (17) Ogawa, H.; Nishikawa, M.; Abe, A. *J. Appl. Phys.* **1982**, *53*, 4448.
- (18) Barsan, N.; Weimar, U. *J. Electroceram.* **2001**, *7*, 143.
- (19) Baraton, M. I.; Merhari, L. *Mater. Trans.* **2001**, *42*, 1616.
- (20) Kolmakov, A.; Moskovits, M. *Annu. Rev. Mater. Sci.* **2004**, *34*, 151.
- (21) Kolmakov, A.; Zhang, Y. X.; Cheng, G. S.; Moskovits, M. *Adv. Mater.* **2003**, *15*, 997.
- (22) Comini, E.; Faglia, G.; Sberveglieri, G.; Pan, Z. W.; Wang, Z. L. *Appl. Phys. Lett.* **2002**, *81*, 1869.
- (23) George, S. M.; Ott, A. W.; Klaus, J. W. *J. Phys. Chem.* **1996**, *100*, 13121.
- (24) Suntola, T. *Thin Solid Films* **1992**, *216*, 84.
- (25) Du, X.; Du, Y.; George, S. M. *J. Vac. Sci. Technol., A* **2005**, *23*, 581.
- (26) Tarre, A.; Rosental, A.; Aidla, A.; Aarik, J.; Sundqvist, J.; Harsta, A. *Vacuum* **2002**, *67*, 571.
- (27) Virola, H.; Niinisto, L. *Thin Solid Films* **1994**, *249*, 144.
- (28) Elam, J. W.; George, S. M. *Chem. Mater.* **2003**, *15*, 1020.
- (29) Ferguson, J. D.; Weimer, A. W.; George, S. M. *J. Vac. Sci. Technol., A* **2005**, *23*, 118.
- (30) Ritala, M.; Leskela, M.; Niinisto, L.; Haussalo, P. *Chem. Mater.* **1993**, *5*, 1174.
- (31) Ritala, M.; Leskela, M.; Nykanen, E.; Soininen, P.; Niinisto, L. *Thin Solid Films* **1993**, *225*, 288.
- (32) Niinisto, L.; Paivasaari, J.; Niinisto, J.; Putkonen, M.; Nieminen, M. *Phys. Status Solidi A* **2004**, *201*, 1443.
- (33) Baraton, M. I.; Merhari, L.; Ferkel, H.; Castagnet, J. F. *Mater. Sci. Eng., C* **2002**, *19*, 315.
- (34) Barsan, N.; Ionescu, R. *Sens. Actuators, B* **1993**, *12*, 71.
- (35) Barsan, N.; Weimar, U. *J. Phys.: Condens. Matter* **2003**, *15*, R813.
- (36) Hahn, S. H.; Barsan, N.; Weimar, U.; Ejakov, S. G.; Visser, J. H.; Soltis, R. E. *Thin Solid Films* **2003**, *436*, 17.
- (37) Baraton, M. I.; Merhari, L. *Scr. Mater.* **2001**, *44*, 1643.
- (38) Kahn, A. H. *Phys. Rev.* **1955**, *97*, 1647.
- (39) Du, Y.; Du, X.; George, S. M. *Thin Solid Films* **2005**, *491*, 43.
- (40) Du, Y.; Du, X.; George, S. M. *J. Phys. Chem. C* **2007**, *111*, 219.
- (41) Ballinger, T. H.; Wong, J. C. S.; Yates, J. T. *Langmuir* **1992**, *8*, 1676.
- (42) Ferguson, J. D.; Weimer, A. W.; George, S. M. *Thin Solid Films* **2000**, *371*, 95.
- (43) Cao, L. X.; Huo, L. H.; Ping, G. C.; Wang, D. M.; Zeng, G. F.; Xi, S. Q. *Thin Solid Films* **1999**, *347*, 258.
- (44) Kersen, U.; Sundberg, M. R. *J. Electrochem. Soc.* **2003**, *150*, H129.
- (45) Alterkop, B.; Parkansky, N.; Goldsmith, S.; Boxman, R. L. *J. Phys. D: Appl. Phys.* **2003**, *36*, 552.
- (46) Baraton, M. I.; Merhari, L. *J. Nanoparticle Res.* **2004**, *6*, 107.
- (47) Jones, R. D.; Summerville, D. A.; Basolo, F. *Chem. Rev.* **1979**, *79*, 139.
- (48) Busca, G. J. *Mol. Struc. (Theochem)* **1983**, *14*, 11.
- (49) Herzberg, G. *Molecular Spectra and Molecular Structure: II. Infrared and Raman Spectra of Polyatomic Molecules*; Van Nostrand Reinhold Company: New York, 1945; p 273.
- (50) Schmid, W.; Barsan, N.; Weimar, U. *Sens. Actuators, B* **2004**, *103*, 362.
- (51) Fort, A.; Mugnaini, M.; Rocchi, S.; Serrano-Santos, M. B.; Vignoli, V.; Spinicci, R. *Sens. Actuators, B* **2007**, *124*, 245.